Development of Folate-Superparamagnetic Nanoconjugates for Inhibition of Cancer Cell Proliferation

Zied Ferjaoui, Sara Nahle, Raphaël Schneider, Halima Kerdjoudj, Damien Mertz, Fabienne Quilès, Khalid Ferji, Eric Gaffet, Halima Alem

ADVANCED MATERIALS INTERFACES
Open Access
www.advmatinterfaces.de

Development of Folate-Superparamagnetic Nanoconjugates for Inhibition of Cancer Cell Proliferation

*Zied Ferjaoui, Sara Nahle, Raphaël Schneider, Halima Kerdjoudj, Damien Mertz, Fabienne Quilès, Khalid Ferji, Eric Gaffet, and Halima Alem**

Here, a versatile strategy to engineer smart theranostic nanocarriers is reported. The core/shell nanosystem is composed of a superparamagnetic iron oxide ($Fe_{3-\delta}O_4$) nanoparticle (NP) core bearing the biocompatible thermo-responsive poly(2-(2-methoxy)ethyl methacrylate-oligo(ethylene glycol methacrylate), P(MEO_2MA_x-$OEGMA_{100-x}$) copolymer (where *x* and 100-*x* represent the molar fractions of MEO_2MA and OEGMA, respectively). Folic acid (FA) is end-conjugated to the P(MEO_2MA_x-$OEGMA_{100-x}$) copolymer, leading to $Fe_{3-\delta}O_4$@P(MEO_2MA_x-$OEGMA_{100-x}$)-FA, to facilitate active targeting of NPs to cancer cells. A highly potent hydrophobic anticancer agent doxorubicin (DOX) is incorporated in the thermo-responsive P(MEO_2MA_x-$OEGMA_y$) brushes via supramolecular interactions to increase its solubility and the assessment of therapeutic potentials. These experiments confirm the magnetic hyperthermia properties of nanocarrier and reveal that only a small amount (10% ± 4%) of DOX is diffused at room temperature, while almost full drug (100%) is released after 52 h at 41 °C. Interestingly, it is found that P(MEO_2MA_{60}-$OEGMA_{40}$) polymers offer to NPs a promising stealth behavior against Human Serum Albumin and Fibrinogen model proteins.

1. Introduction

Ovarian cancer is one of the most common diseases affecting women worldwide. Various chemical drugs such as 5-fluorouracil (5-FU), paclitaxel, cytoxan, and doxorubicin (DOX) are widely employed for treating ovarian cancer.[1] Nevertheless, anticancer agents have potential side effects such as hair loss, infertility, diarrhea, and nausea.[2,3] To minimize these side effects, various types of controlled drug delivery systems have been engineered to specifically target the drug to cancer cells based on cells surface receptors interactions in order to avoid toxicity toward normal cells.[4,5]

Superparamagnetic iron oxide nanoparticles (SPIONs) have been developed extensively due to their wide spectrum of applications in the biomedical field, including biosensors,[6,7] tissue engineering,[8] drug delivery,[9,10] and in medical science for magnetic resonance imaging (MRI).[11,12,13] Another interesting property deals with the fact that they can generate heat upon application of a local high frequency alternating magnetic field (HAMF). The latter is particularly interesting when considering the cancer therapy as the tumors cannot survive heating up to 45 °C.[14] Furthermore, due to their nanosize, SPIONs can easily play with the enhanced permeability and retention (EPR) effect to be delivered to the solid tumor.[15] Moreover, their surface can be easily modified both to specifically direct a cargo

Z. Ferjaoui, S. Nahle, E. Gaffet, H. Alem
Université de Lorraine
CNRS
IJL (UMR 7198)
F-54000 Nancy, France
E-mail: halima.alem@univ-lorraine.fr
R. Schneider
Université de Lorraine
CNRS
LRGP (UMR 7274)
F-54000 Nancy, France
H. Kerdjoudj
Université de Reims Champagne Ardenne
Biomatériaux et Inflammation en Site Osseux (BIOS) EA 4691
F-51100 Reims, France
D. Mertz
Université de Strasbourg
CNRS
Institut de Physique et Chimie des Matériaux de Strasbourg (UMR 7504)
F-67034 Strasbourg, France
F. Quilès
Université de Lorraine
CNRS
LCPME (UMR 7564)
F-54000 Nancy, France
K. Ferji
Université de Lorraine
CNRS
LCPM (UMR 7375)
F-54000 Nancy, France
H. Alem
Institut Universitaire de France
Nancy, France

The ORCID identification number(s) for the author(s) of this article can be found under https://doi.org/10.1002/admi.202202364.

DOI: 10.1002/admi.202202364

molecule to cancer cells and to enhance their stability in biological media.[16]

It is well reported that ovarian cancer cells overexpress the folate alpha receptors (FR-α).[17] Thus, the grafting of folic acid (FA) at the surface of nanocarrier is an interesting strategy to target specifically ovarian cancer cells. This allows to reduce the concentration of injected toxic drugs and to avoid toxicity toward normal cells.[17] Recently, this promising strategy has grasp interest of some research groups. As for example, Pamela et al.[18] prepared magnetic nanotheranostics iron oxide NPs functionalized with FA and loaded with DOX as a therapeutic agent, whereas Wu's group developed a yolk-like Fe_3–$_\delta O_4$–PEI@Gd_2O_3 nanoplatform further functionalized with poly(ethylene glycol) (PEG) and FA for T_1–T_2 dual-mode MRI and cisplatin delivery activated at pH 4.5. The drug-loaded nanoplatform showed better performance on tumor regression than that of free cisplatin.[19] However, controlling the release of the incorporated DOX remains the main limitation of these works.

Grafting thermoresponsive polymers on SPIONs is an attractive strategy to control drug delivery. Thermo-responsive polymers are known to exhibit either an upper critical solution temperature (UCST)[20] or a lower critical solution temperature (LCST).[21] For the former, the polymers that are insoluble in water become soluble above the UCST. In the opposite, for the latter, the polymer chains exhibit a conformational transition from coil to globule above the LCST.[22] Consequently, the use of thermo-responsive polymers displaying a LCST in a temperature range of 40–42 °C is of high interest to design core/shell NPs for biomedical applications.[21] Once these specific macromolecules are covalently grafted at the surface of SPIONs, they could trap an anticancer drug by supramolecular interactions below the physiological temperature. Moreover, their hydrophilicity could increase both the good dispersion and the circulation of SPIONs in the blood.[23,24] The spatio-temporal control release of the loaded drugs could be triggered by heating locally at 40–42 °C.[24,25]

In the present study, we developed smart core/shell NPs (NPs-FA) combining superparamagnetic iron core-coated thermoresponsive polymer brushes for loading and controlling the drug release and FA for active targeting. The system was composed of $Fe_{3-\delta}O_4$ NPs core coated with FA-end functionalized P(MEO_2MA_x-$OEGMA_{100-x}$) copolymer (where x and 100–x represent the molar fractions of 2-(2-methoxy) ethyl methacrylate [MEO_2MA] and oligo (ethylene glycol) methacrylate [OEGMA], respectively), loaded with DOX as an anti-cancer drug. Such NPs will be termed as $Fe_{3-\delta}O_4$@P(MEO2MA_x-$OEGMA_{100-x}$)-FA NPs in this manuscript. The thermo-responsive polymer was engineered to display a LCST around 41 °C in physiological media (PM), above the temperature required for living cells in normal conditions. $Fe_{3-\delta}O_4$@P(MEO2MA_x-$OEGMA_{100-x}$)-FA NPs were characterized by several spectral, diffraction, and microscopic techniques to confirm their nanostructure and their chemical composition as well as their magnetic hyperthermia properties. In vitro studies indicated that $Fe_{3-\delta}O_4$@P(MEO_2MA_{60}-$OEGMA_{40}$)-FA (NPs-FA) were not cytotoxic to normal cells up to a concentration of 100 μg mL^{-1}. The targeting properties of the FA conjugated nanoparticles were investigated toward SKOV-3 cells (ovarian carcinoma cells) and confirmed by confocal microscopy. Interestingly, we found that P(MEO_2MA_{60}-$OEGMA_{40}$) polymers offer to our NPs a promising stealth behavior against human serum albumin (HSA) and fibrinogen (Fbg) model proteins. We believe that those NPs are then for interest for further use in cancer therapy.

2. Results and Discussion

2.1. Characterization of Functionalized Nanocarrier

The synthesis of SPIONs coated with the thermosensitive copolymer has been carried out following a method previously reported by our group.[23,26] Compendiously, SPIONs were synthesized by coprecipitation of iron(III) chloride hexahydrate and iron(II) sulfate heptahydrate following the process described in the Supporting information. Stable hydrophobic NPs of 10 nm of diameter and a superparamagnetic behavior were obtained.[23] Then, a surface initiated radical polymerization from the SPIONs surface was carried out by growing a responsive copolymer based on MEO_2MA and OEGMA monomers. Polymer chains were grown in a controlled fashion by using activators regenerated by electron transfer–atom transfer radical polymerization (ARGET–ATRP) in the presence of $CuBr_2$/Tris(2-pyridylmethyl)amine (TPMA) as catalyst and hydrazine as reducing agent. Two MEO_2MA/OEGMA molar ratios of 60/40 and 65/35 were targeted to prepare polymers exhibiting LCST around 40 °C in physiological media. A targeted release temperature was chosen to be above the body temperature to avoid the aggregation of the NPs when they were injected in the body. Above the LCST, the NPs surface starts to be hydrophobic, which leads to the aggregation of the NPs; hence, when transposed to the body, it leads to a possible thrombosis. The final responsive core/shell NPs will be named in the whole manuscript as $Fe_{3-\delta}O_4$@P(MEO_2MA)$_{60}$-P(OEGMA)$_{40}$ and $Fe_{3-\delta}O_4$@P(MEO_2MA)$_{65}$-P(OEGMA)$_{35}$ corresponding to the 60/40 and 65/35 molar fractions of MEO_2MA/OEGMA, respectively. Last, FA was grafted onto the polymer chain end (**Figure 1**) to ensure the targeting of ovarian cancer cells.

2.1.1. NPs Chemical and Morphological Characterization

$Fe_{3-\delta}O_4$@P(MEO_2MA)$_x$-P(OEGMA)$_{100-x}$ NPs were characterized using various techniques, including high-resolution transmission electron microscope (HR-TEM), X-ray diffraction (XRD), dynamic light scattering (DLS), and infrared spectroscopy (FT-IR).

The chemical signature of the $Fe_{3-\delta}O_4$@P(MEO_2MA_x-$OEGMA_{100-x}$) can be seen in the FT-IR spectra (Figure S1, Supporting Information); the vibration mode of the $Fe_{3-\delta}O_4$ is illustrated by the peak at 575–585 cm^{-1}. The efficiency of the polymerization of the P(MEO_2MA_x-$OEGMA_{100-x}$) from the NPs surface is demonstrated by the absorption bands in 1720 and 1110 cm^{-1} related to the ester C=O and C−O bonds stretching, respectively. The grafting of FA is confirmed by a typical aromatic C=C stretching between 1600 and 1450 cm^{-1}. The sharp aromatic C−N peak at 1350 cm^{-1} and the N−H out of plane

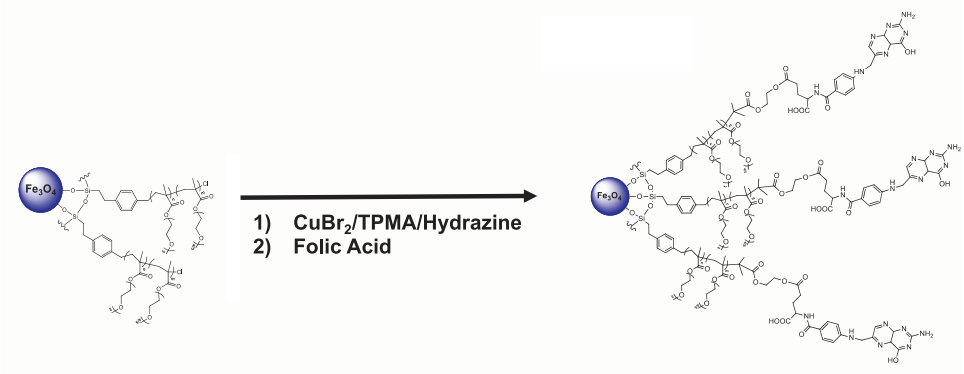

Figure 1. Schematic illustration of the synthetic process for the preparation of $Fe_{3-\delta}O_4$@P(MEO_2MA_x-$OEGMA_{100-x}$)-FA NPs.

vibration at 700 cm^{-1} attest of the radical grafting of the targeting ligand at the NPs chain end. The reader can refer to the Supporting Information and to Ferjaoui et al.[27,23] for full characterization of each synthetic step.

The XRD patterns presented in Figure S2, Supporting Information display sharp and clearly defined peaks demonstrating the high degree of crystallinity of the NPs. The XRD peaks match with the presence of a spinel iron oxide phase. The calculated lattice parameter is 0.841 nm by comparison with those of Fe_3O_4 magnetite phase (0.8396 nm, JCPDS PDF no. 00-019-0629) and the maghemite one γ-Fe_2O_3 (0.8346 nm, JCPDS file 39–1346). By the application of the Scherrer equation, a mean crystallite size of 11.3 nm was calculated from the XRD pattern (broadening of the [311] reflection signal) core (Figure S2, Supporting Information). The size was confirmed by TEM (**Figure 2**a). As shown in Figure 2b, HR-TEM images show round-shaped particles with a core/shell structure and SPIONs in their core leading to diffraction point in the inset present in Figure 2d (Figure 2b; Figure S1, Supporting Information). The presence of the polymer is confirmed by the chemical mapping at the surface of the NP where the Carbon (C) element is mapped in Figure 2c. Moreover, electron diffraction image (insert in Figure 2b) shows concentric circles, associated with crystal planes (200), (311), (400), (422), (511), and (440), which correspond to those of magnetite. These results definitely confirm that the functionalized NPs are well-crystallized over their entire volume at each of the grafting steps. The combination of transmission microscopy and X-ray diffraction confirms that the functionalization steps have no influence on the crystal structure of the nanoparticles.

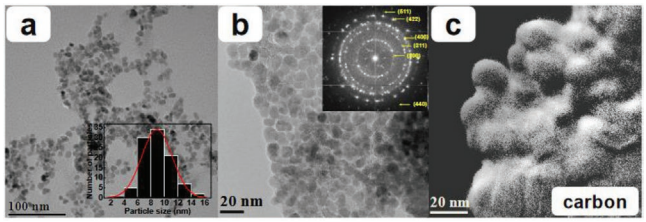

Figure 2. a,b) Bright field TEM micrographs of $Fe_{3-\delta}O_4$@P(MEO_2MA_{60}–$OEGMA_{40}$)-FA NPs (with an image of the electron diffraction in a selected area) and c) C mapping images of $Fe_{3-\delta}O_4$@P(MEO_2MA_{60}–$OEGMA_{40}$)-FA NPs obtained by EF-TEM.

2.1.2. NPs Colloidal Stability in Physiological Media

The responsive behavior is provided by the macromolecular properties of the grafted copolymer chains. They exhibit a LCST of 38 °C and 41 °C for $Fe_{3-\delta}O_4$@P(MEO_2MA_{60}-$OEGMA_{40}$)-FA and for $Fe_{3-\delta}O_4$@P(MEO_2MA_{65}-$OEGMA_{35}$)-FA, respectively, as assessed by the slope change in the DLS monitoring graphs (**Figure 3**). The NPs hydrodynamic diameter is first small and stable in the range of temperature below the LCST (T < LCST). As soon as the LCST is reached, the curve slope changes drastically and their diameter starts to increase, attesting the beginning of the NPs aggregation process. Indeed, when the solution temperature exceeds the LCST (T > LCST), the macromolecules collapse at the surface of the NPs, rendering it hydrophobic. This led to the aggregation of the NPs in the physiological media[26] as illustrated in Figure 3b.

2.1.3. NPs Superparamagnetic and Magnetic Hyperthermia Properties

The superparamagnetic properties of the SPIONs were studied and are shown in Figure S3, Supporting Information. The saturated magnetization of the $Fe_{3-\delta}O_4$@ P(MEO_2MA_{60}-$OEGMA_{40}$)-FA and $Fe_{3-\delta}O_4$@ P(MEO_2MA_{65}-$OEGMA_{35}$)-FA NPs were of 20 and 25 emu g^{-1}, respectively. The saturated magnetization was lower than that obtained generally for the uncoated $Fe_{3-\delta}O_4$ NPs (≈80 emu g^{-1}) due to the magnetic interaction with the diamagnetic copolymer coating[23] (Figure S3a, Supporting Information). The superparamagnetic behavior can be seen in Figure S3a, Supporting Information, as when no magnetic field is applied, there is no magnetization. As shown in Figure S3b, Supporting Information, it is confirmed by ZF/ZFC measurements that the ZF and ZFC curves are crossing at 270K (+/−3 °C), which confirms the superparamagnetic properties of the NPs at room and human body temperature.

2.2. Hyperthermia Study

In vitro DMEM suspensions of $Fe_{3-\delta}O_4$@P(MEO_2MA_{60}-$OEGMA_{40}$)-FA and $Fe_{3-\delta}O_4$@ P(MEO_2MA_{65}-$OEGMA_{35}$)-FA NPs at a concentration of 4.5 mg.mL^{-1} were submitted to an

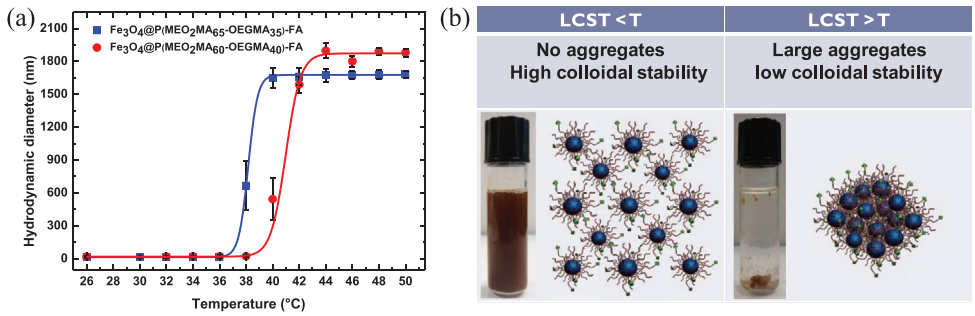

Figure 3. a) Evolution of the hydrodynamic diameter of $Fe_{3-\delta}O_4$@P(MEO_2MA_x-$OEGMA_{100-x}$)-FA NPs in DMEM by heating from 25 °C to 70 °C (heating rate 1 °C min^{-1}). b) The NP dispersions in DMEM below (37 °C) and above (42 °C) the LCST are illustrated in the left and right, respectively. For the sake of clarity, we have pictured the NPs dispersion and aggregation in solution in a clear DMEM better than the red one in (b).

AMF with a frequency F of 536.5 kHz and field amplitude H of 300 Oe. As shown in **Figure 4**, the solution temperature rises were ≈10 °C within 6 min, which translated into a SAR of 38.69 and 92.49 W g^{-1} and resulted in an ILP of 0.24 and 0.57 nHm^2 kg^{-1} as summarized in **Table 1**. Despite the low SPIONs concentration used here, the intrinsic loss power (ILP) values were comparable to commercially available ferrofluids with ILP values ranging from 0.15 to 3.1 nHm^2 K^{-1}.[28,29] The concentration of SPIONs of 4.5 mg mL^{-1} used to determine their heating abilities was lower than that used by most other research groups, as the average concentration of 112 mg_{Fe} mL^{-1} used by Jordan et al.[30,31] for clinical trials, for example. Therefore, if higher temperatures were needed to be reached in a shorter time, increasing the concentration of the SPIONs in suspension could be envisioned.

For the sake of clarity, Table 1 gathers the physical properties of the two materials.

2.3. NPs-FA-Loaded DOX Stability

Those nanosystems are aimed to be used as nanocarrier for cancer therapy; both the stabilities, i.e., the NP suspension and the drug (here Doxorubicin, DOX) entrapment should be guaranteed in physiological media. In **Figure 5**, the stability as a function of time at 37 °C of the NPs with and without the DOX loading is shown. No significant change of the diameter and the PDI over time (up to 72 h) is noticed in DMEM for both NPs, which is further confirmed by the high stability of the solutions as shown in Figure 5b. Note that these experiments were performed at room temperature due to the LCST of Fe_3O_4@P(MEO_2MA_{65}-$OEGMA_{35}$)-FA estimated close to 37 °C (Figure 3a, Table 1).

The drug release properties were monitored at 37 °C (body temperature, below the LCST) and 41 °C (above the LCST) (**Figure 6**). As expected, the release process at 37 °C was much slower than at 41 °C in physiological media.

At 37 °C, the initial proportion of DOX cumulative release from $Fe_{3-\delta}O_4$@P(MEO_2MA_{60}-$OEGMA_{40}$)-FA NPs was less than 10% within almost 10 h (Figure 6). The curve slope started to change after ≈25 h, indicating that the drug can be released even though before the LCST. This is in good agreement with our previous work[27] and is related to the complex composition of the culture media such as proteins and salts that may display kosmotropic effect,[23] inducing the early DOX-polymer hydrogen bond breaking with time. The maximum amount of the DOX release (80%) was reached after 60 h. This first study was essential for the next step which would consist in the in

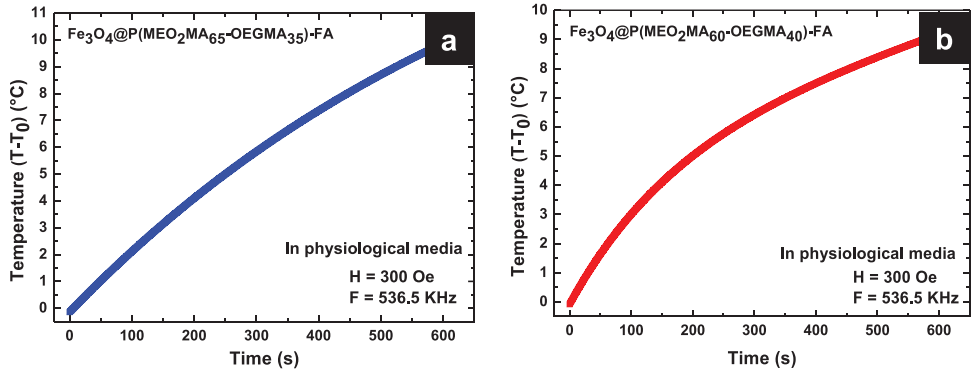

Figure 4. Temperature of $Fe_{3-\delta}O_4$@P(MEO_2MA_x-$OEGMA_{100-x}$)-FA NPs under the AC magnetic field. a) Fe_3O_4@P(MEO_2MA_{65}-$OEGMA_{35}$)-FA, b) Fe_3O_4@P(MEO_2MA_{60}-$OEGMA_{40}$)-FA (T is the measured solution temperature, and T_0 is the temperature of the solution before the application of the magnetic field).

Table 1. Physical characteristics of $Fe_{3-\delta}O_4$@P(MEO2MA)$_{60}$-P(OEGMA)$_{40}$ and $Fe_{3-\delta}O_4$@P(MEO$_2$MA)$_{65}$-P(OEGLMA)$_{35}$.

Materials	$Fe_{3-\delta}O_4$@P(MEO2MA)$_{60}$-P(OEGMA)$_{40}$	$Fe_{3-\delta}O_4$@P(MEO2MA)$_{65}$-P(OEGMA)$_{35}$
LCST	38 °C	41 °C
Saturated magnetization	20 emu g^{-1}	25 emu g^{-1}
ILP	0.24 nHm^2 K^{-1}	0.57 nHm^2 K^{-1}
SAR	38.69 W g^{-1}	92.49 W g^{-1}

vitro study of the core/shell NPs as they could release a small amount of drug even though at a temperature significantly lower than the expected LCST.

Figure 6 shows the evolution of the cumulative drug release (%) with time at 37 °C (physiological temperature and below the LCST) and at 42 °C (above the LCST). Below the LCST, at 37 °C, the DOX was almost not released (0–10% of cumulative release) but after ≈28 h, the slope of the graph changed drastically and a fast and linear increase of the drug release amount was observed. This corresponds to the hydrogen bond between the DOX and the C—O bond of the polymer breaking due to the kosmotropic effect of the salts of the culture media. At 41 °C, a linear increase of the drug release with time was observed. As for the studies conducted at 37 °C, the drug release profile with time was not an on/off system. An initial burst release of 25% was observed for the $Fe_{3-\delta}O_4$@P(MEO$_2$MA$_{60}$-OEGMA$_{40}$)-FA NPs followed by a linear increase with time until reaching 100% after 54 h.

The release kinetics and mechanism of DOX from the magnetic NPs were determined according to the mathematical models described in the Supporting Information. The release parameters for each model (K_1, K_h, K_{kp}, and n) are shown in Table S1, Supporting Information as well as the correlation values (R^2). The Higuchi and the Korsmeyer–Peppas kinetics models do not fit well with the experimental data as indicated by the low R^2 values, whereas the first order kinetics seems to be the best illustrating model for our systems at the 37 °C and the Zero Order for 41 °C.

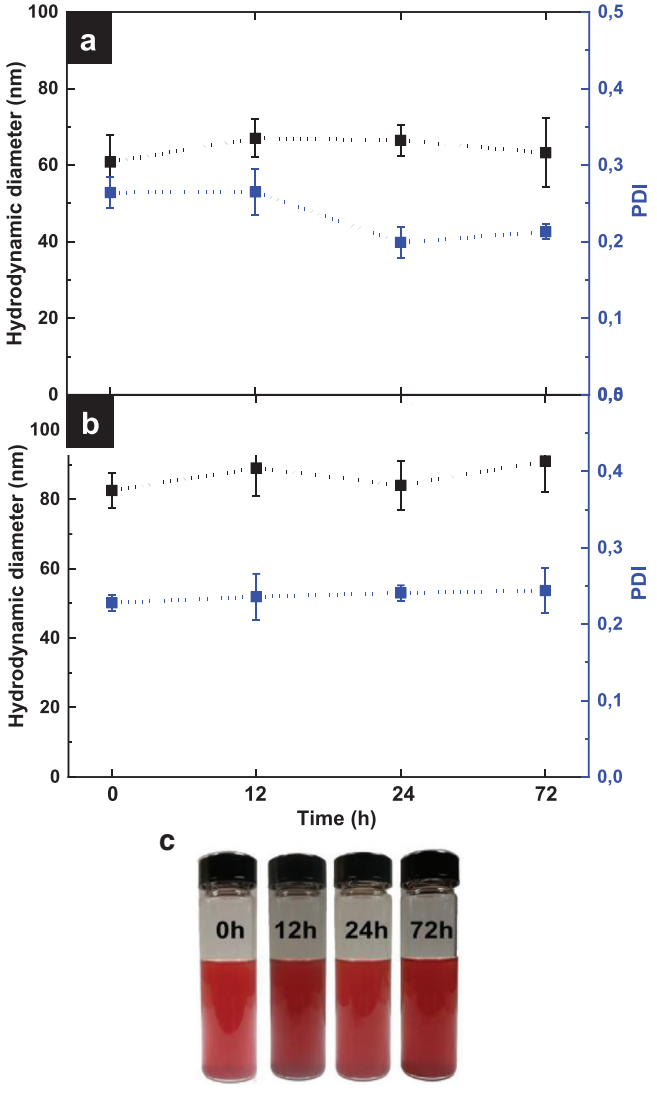

Figure 5. Evolution of the hydrodynamic diameter and the polydispersity index (PDI) of $Fe_{3-\delta}O_4$@P (MEO$_2$MA$_{60}$-OEGMA$_{40}$)-FA NPs a) without DOX and b) with DOX in DMEM from 0 to 72 h at room temperature. c) Picture of the NPs suspension in DMEM from 0 to 72 h with DOX.

2.4. Cytotoxicity Study of $Fe_{3-\delta}O_4$@P(MEO$_2$MA$_{60}$-OEGMA$_{40}$)-FA NPs

2.4.1. Cytotoxicity Toward Ovarian Cancer Line SKOV3

The cytotoxicity of $Fe_{3-\delta}O_4$@P(MEO$_2$MA$_{60}$-OEGMA$_{40}$)-FA NPs was evaluated by the conventional WST-1 assays after incubation with SKOV3 cells for 24 and 72 as it displayed a LCST close to 42 °C, so largely higher than the body temperature. In **Figure 7**, the cell viability after 24 or 72 h of exposure to the NPs is shown. The magnetic core/shell NPs do not exhibit a dose dependent cytotoxicity up to 100 µg mL^{-1} both after 24 and 72 h incubation (Figure 7).

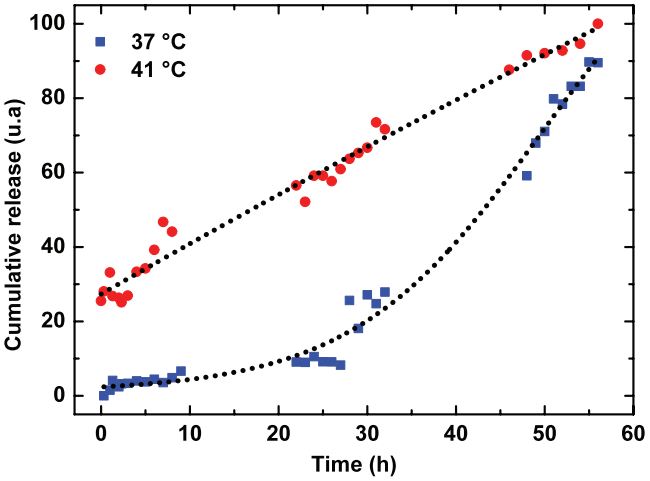

Figure 6. Release of DOX from $Fe_{3-\delta}O_4$@P(MEO$_2$MA$_{60}$-OEGMA$_{40}$)-FA NPs in physiological media (DMEM) at 37 °C and 41 °C.

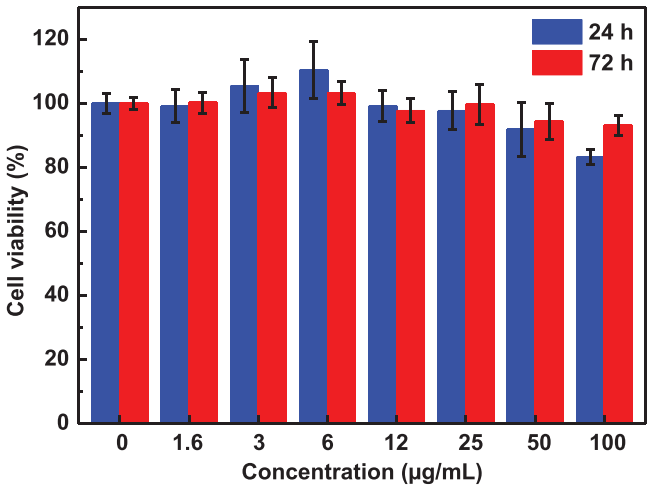

Figure 7. Viability of SKOV3 cells after a) 24 h (blue bars) and b) 72 h (red bars) of exposure to $Fe_3{-}_\delta O_4$@P(MEO_2MA_{60}-$OEGMA_{40}$)-FA NPs.

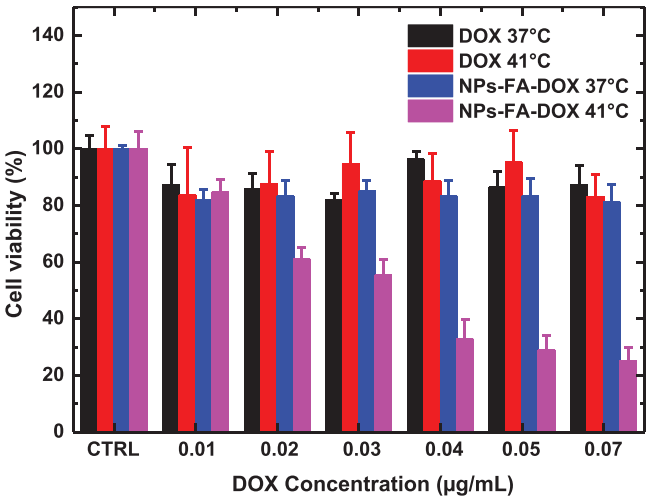

Figure 8. Viability of SKOV-3 cells after 5 h of exposure to DOX loaded $Fe_3{-}_\delta O_4$@P(MEO_2MA_{60}-$OEGMA_{40}$)-FA NPs at 37 °C or 41 °C and free DOX at 37 °C.

2.4.2. Cytotoxicity of DOX Loaded in $Fe_3{-}_\delta O_4$@P(MEO_2MA_{60}-$OEGMA_{40}$)-FA

In vitro cytotoxicity of the DOX loaded in NPs-FA was examined in the SKOV3 cell lines (human ovarian carcinoma cell line), with a broad range of DOX concentrations (0.01–0.07 µg). $Fe_3{-}_\delta O_4$@P (MEO_2MA_{60}-$OEGMA_{40}$)-FA showed negligible cytotoxicity with cell viability higher than 97% after 72 h of contact with a solution of 12 µg mL^{-1}. The anticancer activity of the targeted formulation NPs-FA was studied and compared with free drug DOX. The results showed a dose dependent cell killing for DOX-NPs-FA. The outcome of the study revealed in SKOV3 cells, a half maximal inhibitory concentration (IC_{50}) of 0.04, 0.05, and 0.07 µg for free DOX, DOX-$Fe_3{-}_\delta O_4$@P(MEO_2MA_{60}-$OEGMA_{40}$)-FA at 37 °C, and DOX-NPs-FA at 41 °C, respectively. The noticeably lower IC_{50} of the targeted DOX-NPs-FA at 41 °C as compared to the nontargeted free drug DOX was probably due to the folate receptor specific targeting of DOX-NPs-FA.[32] (**Figure 8**).

2.5. In Vitro Internalization Study ($Fe_3{-}_\delta O_4$@P(MEO_2M_{60}-$OEGMA_{40}$)-FA NPs)

Confocal imaging was performed to confirm the internalization of functional NPs with and without FA in SKOV-3 cells. To perform such observations, the SKOV-3 cells were incubated for 3 h with 100 µg.mL^{-1} of NPs with and without FA. The staining with 4′,6-diamidino-2-phenylindole (DAPI, blue) allowed to locate the nuclei of the cells. Confocal images in **Figure 9** indicate that $Fe_{3-}{}_\delta O_4$@P(MEO_2M_{60}-$OEGMA_{40}$)-FA NPs internalize better than $Fe_3{-}_\delta O_4$@P(MEO_2M_{60}-$OEGMA_{40}$). The presence of FA, targeting FRα receptors expressed on the surface of cells, facilitates the internalization of NPs-FA (Figure 9) within cancer cells. It is widely admitted that depending on the species, the nuclear pore complex has an outer diameter of ≈120–130 nm and a height of 50–80 nm.[33,34] Herein, our results suggest that the ovarian cancer cell line has larger pore size diameter then nanoparticles size.

2.6. Interaction of Human Albumin (HSA) and Fibrinogen (Fbg) With $Fe_3{-}_\delta O_4$@P(MEO_2MA_{65}-$OEGMA_{35}$ and $Fe_3{-}_\delta O_4$@P(MEO_2MA_{60}-$OEGMA_{40}$ NPs

The uptake of proteins on nanovectors depends on several parameters, such as their shape, their surface chemical composition, their surface properties, and zeta potential of the NPs.[35] It is well known nowadays that the stealth behavior of PEG coated on NPs prevents from aggregation, opsonization, and phagocytosis, leading to the prolongation of the systemic circulation time. Indeed, PEGylation makes NPs transparent to the immune system as it only "sees" a crown of water.[35] As for example, PEG-grafted Au NPs were studied by Walkey et al. who showed that the density of the PEG grafts could control the uptake of 70 serum proteins. Interestingly, they noticed that increasing the PEG density could lead to the decrease of the adsorbed protein at the NPs surface changing therefore the structure of the protein corona. The grafting of a PEG layer around the NPs has thus shown a promising protein repellent property. However, the PEG grafting density in this work was relatively high (1.25 PEG.nm^{-2}). Nevertheless, the high amount of polymer chains decreased the internalization of the NPs within the cells which can limit their further use in cancer therapy.[36] A balance between the grating density and the cell internalization has then to be considered.

The copolymer used in this study is well known to be protein repellant[37–39] when grafted on surfaces. To understand the interaction between the body protein and the $Fe_3{-}_\delta O_4$@P(MEO_2M_{60}-$OEGMA_{40}$)-FA NPs, in vitro experiments have been conducted by dispersing NPs in physiological solutions containing growing concentrations of Albumin (HSA) and Fibrinogene (Fbg), the most abundant proteins in the blood.

Control $Fe_{3-}{}_\delta O_4$@NH_2 particles were used to study the effects of HSA and Fbg precoating on the particles. We first incubated $Fe_{3-}{}_\delta O_4$@P(MEO_2MA_{65}-$OEGMA_{35}$) and $Fe_{3-}{}_\delta O_4$@P (MEO_2MA_{60}-$OEGMA_{40}$) with various concentrations of HSA and Fbg for 2 h at 37 °C and isolated the proteins adsorbed

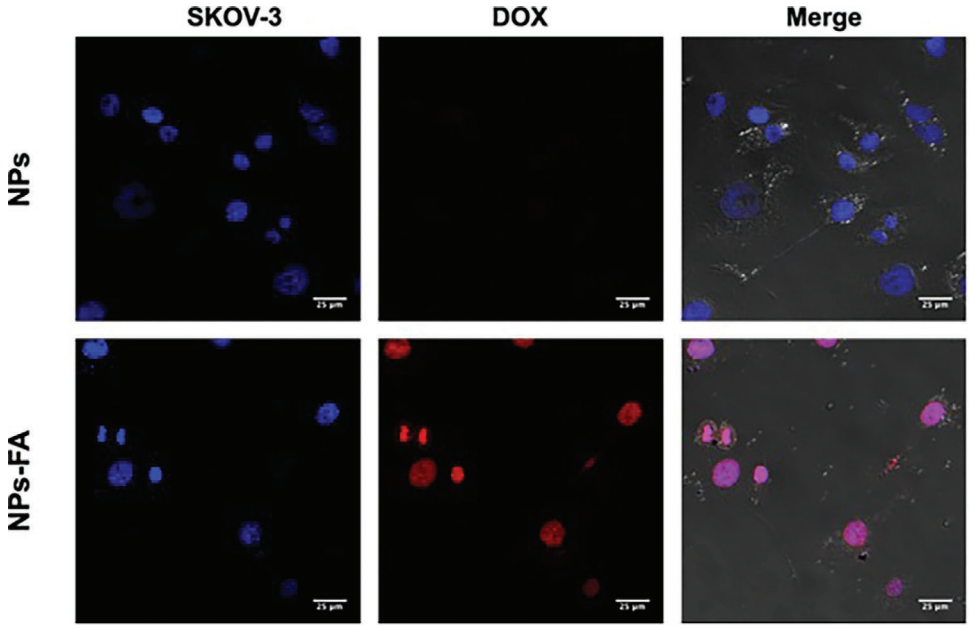

Figure 9. Confocal images of SKOV-3 cells treated with $Fe_{3-\delta}O_4$@P(MEO_2M_{60}-$OEGMA_{40}$) (NPs) and $Fe_{3-\delta}O_4$@P(MEO_2M_{60}-$OEGMA_{40}$)-FA (NPs-FA) loaded with DOX for 3 h. Labeling of nuclei with DAPI (blue).

on them by centrifugation to completely remove the unbound proteins.

To further confirm the particle–protein interactions, they were studied using light scattering (Table S2, Supporting Information) owing to their sensitivity at the nanometric scale. The evolution of the hydrodynamic diameter of the NPs as a function of protein concentration is shown in **Figure 10**.

Concerning the interaction of HSA with the functionalized NP, as seen in the DLS data, the adsorption really occurred when the NPs were in contact in solution of a concentration higher than 2.5 g.L^{-1}. HSA is known to bind and carry fatty acids in the vascular system,[40] which indicates its affinity to hydrophobic interaction, but functional groups such as COOH/COO^-, NH_2/NH_3^+, and OH which are present on HSA sites are able to interact with the NH_2 group of $Fe_{3-\delta}O_4$@NH_2 via electrostatic interactions or hydrogen-bonding with the R—C—O or R—C=O group of the copolymer. In contact with HSA, the hydrodynamic diameters of the NPs increased slowly and almost linearly with the concentration of the HSA (see Figure 9). However, it should be mentioned that the small diameter increase was still in the error bar range, making this interpretation very approximative. As the DLS could not provide a relevant conclusion concerning the adsorption of HSA at the surface of the $Fe_{3-\delta}O_4$@NH_2, FTIR-ATR measurements were performed to confirm these promising results.

Figure 11a shows the FTIR-ATR spectra of $Fe_{3-\delta}O_4$@NH_2 NPs recorded in their PBS media prior to contact with the proteins. Figure S7, Supporting Information shows the FTIR-ATR spectra of HSA and Fbg in the fingerprint region (i.e., between 1800 and 800 cm^{-1}). The two intense bands near 1650 and 1550 cm^{-1} were assigned to amide I and II bands, respectively.[41] The broad band near 1590 cm^{-1} (Figure 10a) was assigned the NH_2 bending band. The spectrum of $Fe_{3-\delta}O_4$@NH_2 NPs after exposure to HSA at 5 g L^{-1} shows two additional bands at 1656 and 1553 cm^{-1}. They were assigned to HSA amide I and II bands, respectively, and they showed the occurrence of HSA on the $Fe_{3-\delta}O_4$@NH_2 NPs. Figure 11b shows the FTIR-ATR spectra of $Fe_{3-\delta}O_4$@P(MEO_2M_{65}-$OEGMA_{35}$) NPs as a control. Bands absorbing at 1723 and 1700 cm^{-1} were assigned to C=O stretchings of the polymer with two different environments (hydrogen bonding). The FTIR-ATR spectra did not allow detecting with confidence the occurrence of HSA even at 5 g L^{-1}. It is concluded that there was a very weak HSA sorption on the $Fe_{3-\delta}O_4$@P(MEO_2M_{65}-$OEGMA_{35}$) NPs. For Fbg, the DLS data shows a high increase of the hydrodynamic diameter. Fbg was not clearly detected at the concentration of 0.5 g L^{-1} (data not shown). However, when $Fe_{3-\delta}O_4$@P(MEO_2M_{65}-$OEGMA_{35}$) NPs were exposed to Fbg at 5 g L^{-1}, bands at 1647 and 1553 cm^{-1} occurred in the FTIR-ATR spectra; they were assigned to Fbg amide I and II bands, respectively. Amide bands are sensitive to the secondary structure of the proteins.[40] The wavenumbers were in accordance with the secondary structure of Fbg that was a mixture of α helices and β sheets. In addition, the band at 1700 cm^{-1} from $Fe_{3-\delta}O_4$@P(MEO_2M_{65}-$OEGMA_{35}$) NPs disappeared. It suggested that esters C=O bond was implied in the interaction with Fbg.

Concerning the Fbg adsorption, a remarkable increase of the$Fe_{3-\delta}O_4$@NH_2 NPs diameter in the order of 70 nm at a concentration of 5 g L^{-1} of Fbg was noticed. This increase could be explained by: i) on the one hand, the formation of NH_3^+ for the $Fe_{3-\delta}O_4$@NH_2 NPs and the presence of negative charges for Fbg,[42] which favors the electrostatic interaction between the $Fe_{3-\delta}O_4$@NH_2 NPs and Fbg[42], ii) and, on the other hand, to the high concentration of Fbg (5 g L^{-1}) where the Fbg molecules adsorb onto the silane layer and presumably self-assemble thereafter, forming a thick layer on the surface of

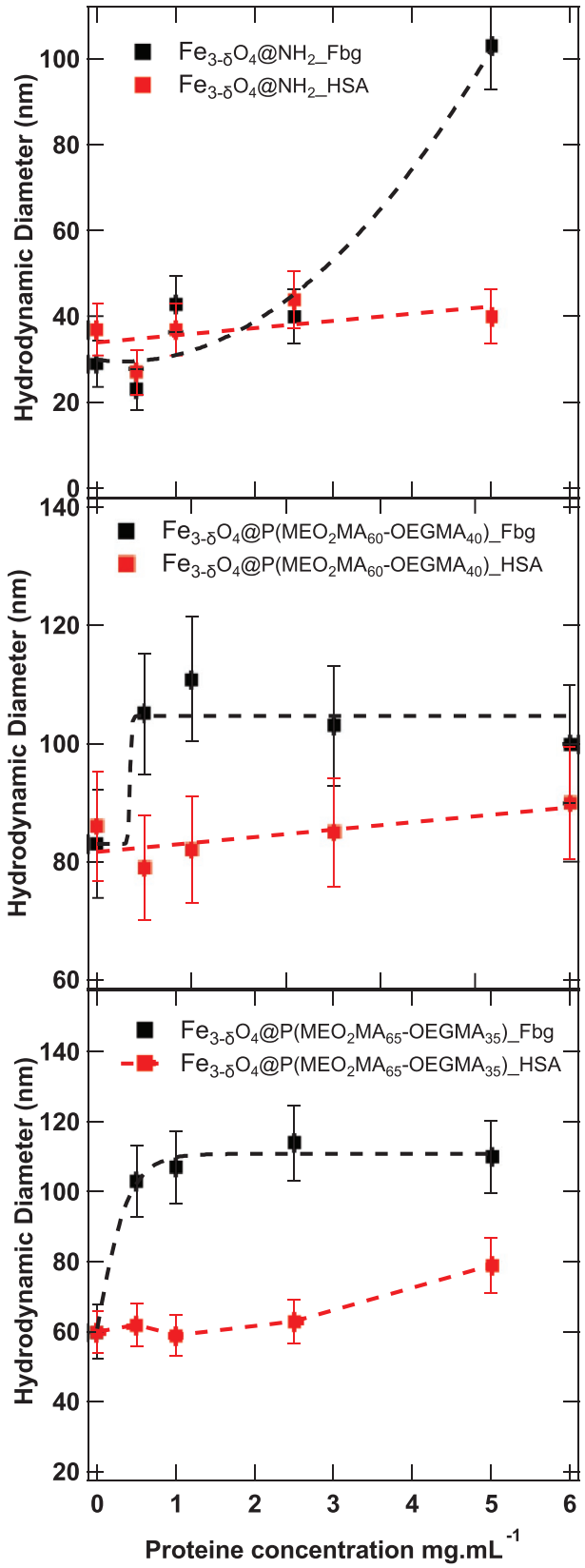

Figure 10. Evolution of the hydrodynamic diameter of the a) $Fe_3{-}_\delta O_4$@NH_2, b) $P(MEO_2MA_{60}$-$OEGMA_{40})$, and c) $P(MEO_2MA_{65}$-$OEGMA_{35})$ as a function of protein concentration.

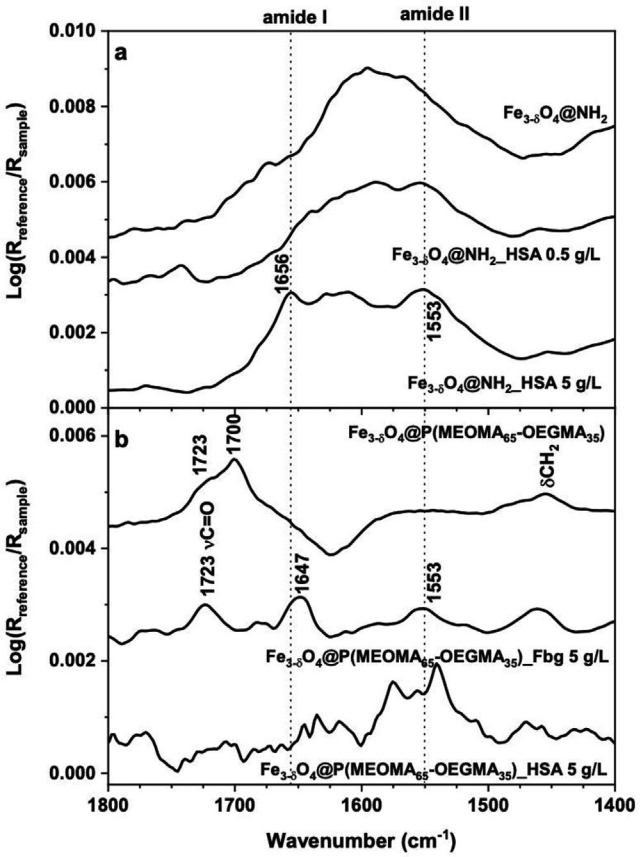

Figure 11. FTIR-ATR spectra of a) $Fe_3{-}_\delta O_4$@NH_2 NPs not exposed and after exposure to HSA at 0.5 and 5 g L^{-1} and b) $Fe_3{-}_\delta O_4$@$P(MEO_2M_{65}$-$OEGMA_{35})$ not exposed and after exposure to HSA or Fbg at 5 g L^{-1} (reference = PBS medium).

the NP with a size of ≈37 nm. The difference in size between these NPs before and after contact with a 5 mg mL^{-1} solution was close to the size of the Fbg protein (45 nm).[43] As soon as the Fbg was in contact with the copolymer grafted NPs, a slight increase of the Fbg amount adsorbed was observed from 0.5 g.L^{-1} where the hydrodynamic diameter was increased by ≈20 and 50 nm for the $Fe_3{-}_\delta O_4$@$P(MEO_2MA_{60}$-$OEGMA_{40})$ and $Fe_{3-}{}_\delta O_4$@$P(MEO_2MA_{65}$-$OEGMA_{35})$, respectively. Both sizes were lower than the expected increase of the diameter if a monolayer of fibrinogen was adsorbed at the surface (expected increase of ≈90 nm without taking into account the hydration sphere; all the DLS data are summarized in Table S2, Supporting Information). This can be explained by the fact that Fbg is able to diffuse partially within the polymer chain grafted at the surface of the NPs,[43] which is confirmed by FT-IR as the Fbg is clearly seen at 5 g L^{-1} and not for the concentration of 0.5 g L^{-1} where the protein amount is too low to be detected. By combining DLS and FT-IR investigations, we can assume that the $P(MEO_2MA_{60}$-$OEGMA_{40})$ can prevent the adsorption of the HSA but hardly the Fbg diffusion as it was already demonstrated for poly(ethylene glycol).[43]

Based on these findings, this $P(MEO_2MA_x$-$OEGMA_y)$-FA modified nanovector exhibits an interesting stealth property. The absence of protein corona around it, the aggregation, and

high dispersion make these NPs an ideal candidate for cancer treatment and diagnosis.

3. Conclusion

In this study, core/shell NPs for cancer therapy were successfully synthesized with SPIONs as the core and P(MEO_2MA/OEGMA)-FA conjugates as the shell. The engineered magnetic NPs $Fe_{3-\delta}O_4$@P (MEO_2MA_{60}-$OEGMA_{40}$)-FA showed great potential to be a promising anticancer drug delivery system for DOX. The targeted NPs $Fe_{3-\delta}O_4$@P(MEO_2MA_{60}-$OEGMA_{40}$)-FA possessed numerous favorable characteristics such as improved aqueous dispersibility for delivering a high dose of DOX with high specificity to target cancer cells expressing folate receptors. The stealth properties of $Fe_{3-\delta}O_4$@P(MEO_2M_x-$OEGMA_{100-x}$) were investigated via their contacts with human albumin and fibrinogen enriched solutions. The physicochemical results show that the NPs surface-modified by P(MEO_2M_x-$OEGMA_{100-x}$) did not display signals due to the formation of a crown of the proteins concerning HSA but confirmed the adsorption of fibrinogen.The results demonstrate promising potential of DOX loaded $Fe_{3-\delta}O_4$@P(MEO_2MA_{60}-$OEGMA_{40}$)–FA for simultaneous therapy of folate receptor expressing cancers.

Supporting Information

Supporting Information is available from the Wiley Online Library or from the author.

Acknowledgements

This work was financially supported by the Centre National de Recherche Scientifique (CNRS). The authors are thankful to Dr. Jaafar Ghanbaja for the TEM characterizations within the CC3M/IJL (UMR 7198, Univ Lorraine – CNRS). F.Q. is thankful to the SMI facility of LCPME (UMR 7564, Univ. Lorraine – CNRS) where the FTIR-ATR spectra were recorded. The authors relied on the CC X Gamma/IJL for achieving the XRD diffraction measurements.

Conflict of Interest

The authors declare no conflict of interest.

Data Availability Statement

The data that support the findings of this study are available from the corresponding author upon reasonable request.

Keywords

cells targeting, core/shell nanoparticles, doxorubicin, drug delivery, folic acid, hyperthermia, magnetic nanoparticles, responsive nanomaterials

Received: November 15, 2022
Revised: January 20, 2023
Published online:

[1] W. Zoli, P. Ulivi, A. Tesei, F. Fabbri, M. Rosetti, R. Maltoni, D. C. Giunchi, L. Ricotti, G. Brigliadori, I. Vannini, D. Amadori, *Breast Cancer Res.* **2005**, *7*, R681.
[2] G. Mani, S. Kim, K. Kim, *Biomacromolecules* **2018**, *19*, 3257.
[3] A. E. Kayl, C. A. Meyers, *Curr. Opin. Obstet. Gynecol.* **2006**, *18*, 24.
[4] Y. Hui, D. Wibowo, Y. Liu, R. Ran, H.-F. Wang, A. Seth, A. P. J. Middelberg, C.-X. Zhao, *ACS Nano* **2018**, *12*, 2846.
[5] J. A. Vassie, J. M. Whitelock, M. S. Lord, *Mol. Pharmaceutics* **2018**, *15*, 994.
[6] M. Dolci, J.-F. Bryche, C. Leuvrey, S. Zafeiratos, S. Gree, S. Begin-Colin, G. Barbillon, B. P. Pichon, *J. Mater. Chem. C* **2018**, *6*, 9102.
[7] M. Arvand, M. Sanayeei, S. Hemmati, *Biosens. Bioelectron.* **2018**, *102*, 70.
[8] M. R. A. Abdollah, T. J. Carter, C. Jones, T. L. Kalber, V. Rajkumar, B. Tolner, C. Gruettner, M. Zaw-Thin, J. Baguña Torres, M. Ellis, M. Robson, R. B. Pedley, P. Mulholland, R. T. M. de Rosales, K. A. Chester, *ACS Nano* **2018**, *12*, 1156.
[9] S. Laurent, A. A. Saei, S. Behzadi, A. Panahifar, M. Mahmoudi, *Expert Opin. Drug Delivery* **2014**, *11*, 1449.
[10] X. Sun, R. Du, L. Zhang, G. Zhang, X. Zheng, J. Qian, X. Tian, J. Zhou, J. He, Y. Wang, Y. Wu, K. Zhong, D. Cai, D. Zou, Z. Wu, *ACS Nano* **2017**, *11*, 7049.
[11] F. Yang, A. Skripka, M. S. Tabatabaei, S. H. Hong, F. Ren, A. Benayas, J. K. Oh, S. Martel, X. Liu, F. Vetrone, D. Ma, *ACS Nano* **2019**, *13*, 408.
[12] H. L. Chee, C. R. R. Gan, M. Ng, L. Low, D. G. Fernig, K. K. Bhakoo, D. Paramelle, *ACS Nano* **2018**, *12*, 6480.
[13] J. Yan, S. Li, F. Cartieri, Z. Wang, T. K. Hitchens, J. Leonardo, S. E. Averick, K. Matyjaszewski, *ACS Appl. Mater. Interfaces* **2018**, *10*, 21901.
[14] A. Chicheł, J. Skowronek, M. Kubaszewska, M. Kanikowski, *Rep. Pract. Oncol. Radiother.* **2007**, *12*, 267.
[15] H. Kang, S. Rho, W. R. Stiles, S. Hu, Y. Baek, D. W. Hwang, S. Kashiwagi, M. S. Kim, H. S. Choi, *Adv. Healthcare Mater.* **2020**, *9*, 1901223.
[16] J. Lin, Y. Li, Y. Li, H. Wu, F. Yu, S. Zhou, L. Xie, F. Luo, C. Lin, Z. Hou, *ACS Appl. Mater. Interfaces* **2015**, *7*, 11908.
[17] J. Sudimack, R. J. Lee, *Adv. Drug Delivery Rev.* **2000**, *41*, 147.
[18] P. L. Azcona, M. G. Montiel Schneider, M. Grünhut, V. L. Lassalle, *New J. Chem.* **2019**, *43*, 2126.
[19] J. Jaber, E. Mohsen, *Colloids Surf., B* **2013**, *102*, 265.
[20] P. Lertturongchai, M. I. A. Ibrahim, A. Durand, P. Sunintaboon, K. Ferji, *Macromol. Rapid Commun.* **2020**, *41*, 2000058.
[21] D. Roy, W. L. A. Brooks, B. S. Sumerlin, *Chem. Soc. Rev.* **2013**, *42*, 7214.
[22] R. Hoogenboom, in *Smart Polymers and Their Applications* (Eds: M. R. Aguilar, J. S. Román), Elsevier, Amsterdam, the Netherlands **2014**, pp. 15–44.
[23] Z. Ferjaoui, R. Schneider, A. Meftah, E. Gaffet, H. Alem, *RSC Adv.* **2017**, *7*, 26243.
[24] E. Jamal Al Dine, Z. Ferjaoui, J. Ghanbaja, T. Roques-Carmes, A. Meftah, T. Hamieh, J. Toufaily, R. Schneider, S. Marchal, E. Gaffet, H. Alem, *Int. J. Pharm.* **2017**, *532*, 738.
[25] E. J. A. Dine, Z. Ferjaoui, T. Roques-Carmes, A. Schjen, A. Meftah, T. Hamieh, J. Toufaily, R. Schneider, E. Gaffet, H. Alem, *Nanotechnology* **2017**, *28*, 125601.
[26] H. Alem, A. Schejn, T. Roques-Carmes, J. Ghanbaja, R. Schneider, *Nanotechnology* **2015**, *26*, 335605.
[27] Z. Ferjaoui, E. Jamal Al Dine, A. Kulmukhamedova, L. Bezdetnaya, C. Soon Chang, R. Schneider, F. Mutelet, D. Mertz, S. Begin-Colin, F. Quilès, E. Gaffet, H. Alem, *ACS Appl. Mater. Interfaces* **2019**, *11*, 30610.
[28] C. Blanco-Andujar, D. Ortega, P. Southern, Q. A. Pankhurst, N. T. K. Thanh, *Nanoscale* **2015**, *7*, 1768.

[29] A. E. Dunn, D. J. Dunn, A. Macmillan, R. Whan, T. Stait-Gardner, W. S. Price, M. Lim, C. Boyer, *Polym. Chem.* **2014**, *5*, 3311.
[30] F. K. H. van Landeghem, K. Maier-Hauff, A. Jordan, K.-T. Hoffmann, U. Gneveckow, R. Scholz, B. Thiesen, W. Brück, A. von Deimling, *Biomaterials* **2009**, *30*, 52.
[31] M. Johannsen, U. Gneveckow, B. Thiesen, K. Taymoorian, C. H. Cho, N. Waldöfner, R. Scholz, A. Jordan, S. A. Loening, P. Wust, *Eur. Urol.* **2007**, *52*, 1653.
[32] D. Luong, S. Sau, P. Kesharwani, A. K. Iyer, *Biomacromolecules* **2017**, *18*, 1197.
[33] M. Allegretti, C. E. Zimmerli, V. Rantos, F. Wilfling, P. Ronchi, H. K. H. Fung, C.-W. Lee, W. Hagen, B. Turoňová, K. Karius, M. Börmel, X. Zhang, C. W. Müller, Y. Schwab, J. Mahamid, B. Pfander, J. Kosinski, M. Beck, *Nature* **2020**, *586*, 796.
[34] E. Dultz, M. Wojtynek, O. Medalia, E. Onischenko, *Cells* **2022**, *11*, 1456.
[35] R. Rampado, S. Crotti, P. Caliceti, S. Pucciarelli, M. Agostini, *Front. Bioeng. Biotechnol.* **2020**, *8*, 166.
[36] C. D. Walkey, J. B. Olsen, H. Guo, A. Emili, W. C. W. Chan, *J. Am. Chem. Soc.* **2012**, *134*, 2139.
[37] J.-F. Lutz, Ö. Akdemir, A. Hoth, *J. Am. Chem. Soc.* **2006**, *128*, 13046.
[38] J.-F. Lutz, A. Hoth, *Macromolecules* **2006**, *39*, 893.
[39] X. Laloyaux, E. Fautré, T. Blin, V. Purohit, J. Leprince, T. Jouenne, A. M. Jonas, K. Glinel, *Adv. Mater.* **2010**, *22*, 5024.
[40] G. J. van der Vusse, *Drug Metab. Pharmacokinet.* **2009**, *24*, 300.
[41] J. Kong, S. Yu, *Acta Biochim. Biophys. Sin.* **2007**, *39*, 549.
[42] H. Zhang, T. Wu, W. Yu, S. Ruan, Q. He, H. Gao, *ACS Appl. Mater. Interfaces* **2018**, *10*, 9094.
[43] B. Pelaz, P. del Pino, P. Maffre, R. Hartmann, M. Gallego, S. Rivera-Fernández, J. M. de la Fuente, G. U. Nienhaus, W. J. Parak, *ACS Nano* **2015**, *9*, 6996.